energies

MDPI

Article

Charge and Discharge Analyses of a PCM Storage System Integrated in a High-Temperature Solar Receiver

Ambra Giovannelli * and Muhammad Anser Bashir

Department of Engineering, University of Roma Tre, Via della Vasca Navale 79, 00146 Rome, Italy; muhammadanser.bashir@uniroma3.it

* Correspondence: ambra.giovannelli@uniroma3.it; Tel.: +39-06-57333424

Received: 31 October 2017; Accepted: 20 November 2017; Published: 23 November 2017

Abstract: Solar Dish Micro Gas Turbine (MGT) systems have the potential to become interesting small-scale power plants in off-grid or mini-grid contexts for electricity or poly-generation production. The main challenging component of such systems is the solar receiver which should operate at high temperatures with concentrated solar radiations, which strongly vary with time. This paper deals with the design and the analysis of a novel solar receiver integrated with a short-term storage system based on Phase Change Materials to prevent sudden variations in the maximum temperature of the MGT working fluid. Particularly, the charge and discharge behavior of the storage system was analyzed by means of Computational Fluid Dynamic methods to evaluate the potentiality of the concept and the component capabilities. Achieved results were highly satisfactory: the novel solar receiver has a good thermal inertia and can prevent relevant fluctuations in the working fluid temperature for 20–30 min.

Keywords: concentrated solar power plant; solar receiver; Phase Change Materials (PCM) storage system

1. Introduction

Several technologies based on solar radiation utilization have already been developed for electricity generation at the small scale for off-grid or mini-grid applications [1]. Although Photovoltaic (PV) systems remain the most common technology applied for these purposes [2,3], the low efficiency varying the environmental conditions of commercially available PV panels [4–6] and the requirement of expensive storage devices (e.g., battery units) make Small-Scale Concentrated Solar Power Plants (SS-CSPPs) interesting systems. Nowadays, some SS-CSPPs already exist, as Parabolic Trough Collectors coupled with Organic Rankine Cycle (PTC-ORC) plants and Dish-Stirling engine units [7]. Recently, the availability of new high temperature materials focused the research on the development of new CSPPs as Micro Gas Turbines (MGTs) coupled with solar mini-towers or dishes [8–10]. In the last few years, some projects have been launched to develop SS-CSP systems based on MGT technology [10–12]. The aim has been the development of a reliable system, cheaper than Dish-Stirling units and with a higher efficiency than PTC-ORC or Photovoltaic plants. Nowadays, a prototype unit (up to 10 kWe) has been built and preliminary tests have been carried out to prove the concept [10].

A Dish-MGT system consists of a paraboloidal concentrator, a High-Temperature (HT) solar receiver, and a recuperated MGT connected with a generator, as shown in Figure 1. The solar receiver absorbs the concentrated solar radiation and heats the compressed air coming from the recuperator.

HT solar receivers are the most challenging components in a Dish-MGT system. Such a component has to heat the compressed air up to 800–950 °C (in the absence of a supplementary combustion

chamber) in order to have a high-efficiency recuperated MGT. In the last years, relevant progress has been made in the development of reliable HT receivers.

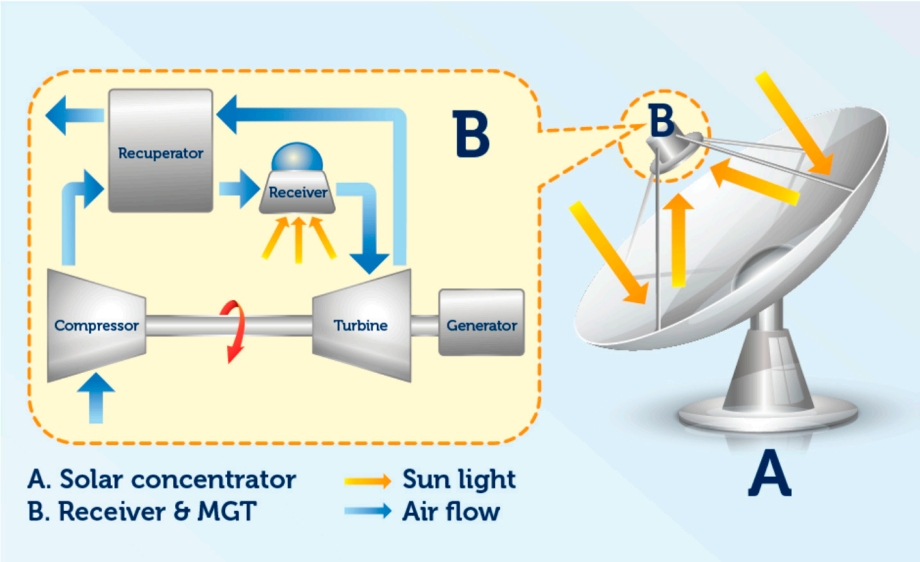

Figure 1. Scheme of a Dish-Micro Gas Turbine concentrating solar power plant [13].

Cavity shaped solar receivers are designed to minimize re-radiation losses and have a better coupling with the concentrated solar flux provided by the dish [14–16]. The Working Fluid (WF) inside the receiver cavity can be heated either directly or indirectly. In solar receivers with a direct WF heating, a quartz window is used to separate the WF from the external environment. In such receiver layouts, the WF can be heated directly by the concentrated solar radiation or there can be an intermediate medium to enhance the heat transfer process (e.g., a porous material, a fluidized bed, a corrugated structure with a wide contact surface). Relevant examples are given in the following papers [17–22]. Mostly volumetric receivers are directly heated, although the quartz window is a critical component in the device layout; it has to be strong enough at HT and relatively thin to reduce radiation absorption [23]. It usually limits the receiver internal pressure and requires an active cooling at temperatures higher than 800 °C [24]. Furthermore, attention has to be paid to maintain clean internal and external window surfaces to avoid hot spots during operating conditions, and differential thermal expansion between the quartz window and the receiver structure has to be strictly limited.

In indirect heating receivers, the concentrated solar radiation heats either an opaque cavity wall or the surface of tubes housed in the device volume. The WF can be heated either by the contact with the cavity wall or by the surface of the tubes in which the WF passes through [25–28]. Tubular configurations are the most common layout arrangement for this kind of receiver. Material degradation is one of the major concerns at HT; therefore, many efforts have been focused to reduce the effect of degradation issues such as creep damage, microstructural degradation, fatigue and creep-fatigue phenomena, erosion, thermal shocks, HT corrosion etc. [29–31]. Nowadays, some promising materials, both metallic and ceramic, show suitable properties to be taken into consideration for HT applications [32–35]. However, in CSPPs another relevant issue in the design of solar receivers concerns the natural fluctuation of the solar radiation. Sudden variations of the solar flux due to clouds or the humidity of fog quickly modify the solar flux, which impinges over the receiver surface, stressing the device structure and causing a fast variation in the WF outlet temperature if the device thermal capacity is low. Such a phenomenon reduces plant performance and, in a Dish-MGT system, can lead to structural damage in the engine.

This paper deals with the design and analysis of a novel HT solar receiver equipped with an integrated short-term storage system based on Phase Change Materials (PCMs). Such a short-term

storage system should increase the receiver thermal capacity and prevent sudden variations of the WF temperature at the device outlet section.

The present work is an extended version of the paper shown at the 4th International Conference on Energy and Environment Research ICEER 2017 held in Porto, Portugal and published in Energy Procedia [36].

2. The Solar Receiver

The reference plant taken into consideration for the present work consists of a recuperated MGT coupled with a Solar Dish. The target electrical power output is about 5–8 kW. Table 1 shows the most relevant boundary conditions which come from a preliminary power cycle analysis. A tubular cavity receiver integrated with PCM for short-term thermal energy storage was designed accordingly. A scheme of the device is shown in Figure 2. The receiver consists of a cylindrical container with 12 U-tubes housed inside the structure and submerged in a PCM. The compressed air comes from the recuperator and flows inside the tubes. Table 2 summarizes some relevant details of the device geometry. The concentrated solar radiation impinges on the receiver front surface, heating the PCM inside the volume. The PCM is an intermediate medium which can store sensible and latent heat and transfers part of the heat to the compressed air inside the U-tubes. On the basis of previous analyses carried out by the authors [37,38], the receiver front surface was shaped with a conical cavity. Such geometry increases the radiation absorption capacity of the receiver reducing the hot wall temperature and, consequently, the re-radiation effects.

To reduce the WF outlet temperature fluctuations caused by the instant variation of the solar radiation, a short-term thermal energy storage system was integrated in the receiver volume. The selection of a suitable PCM for this specific application is very critical and depends on several basic requirements like melting temperature, specific thermal capacity, heat of fusion, density, thermal conductivity, volume change at transition, congruent melting, chemical stability, compatibility with constructional materials, etc. [39,40]. Several salts and metallic compounds show high melting temperatures and can be used for HT applications. Furthermore, some metallic alloys have high thermal conductivity and specific thermal capacity, small volume change, and a good compatibility with other materials [41–44]. For this specific application, the Mg56-Si44 wt % eutectic compound was selected as a PCM due to its promising thermal properties and the small volume change in phase transition. The main properties are reported in Table 3.

Such a receiver configuration comes from a steady-state analysis carried out at nominal conditions. Particularly, 3D Computational Fluid Dynamic (CFD) simulations were carried out, varying some relevant geometric parameters (cavity length, opening and shape) in order to select the most proper receiver configuration. More details are available in a previous publication [38].

Table 1. Reference power plant main conditions.

Power Plant	Value
Electrical power output (kW)	5–8
Turbine Inlet Temperature (K)	1073–1123
Air mass flow (kg/s)	0.065–0.16
Air compressor inlet temperature (K)	288
Air compressor inlet pressure (kPa)	101,325
Compressor pressure ratio	2–3
MGT efficiency (%)	22–29
Expected receiver efficiency (%)	60

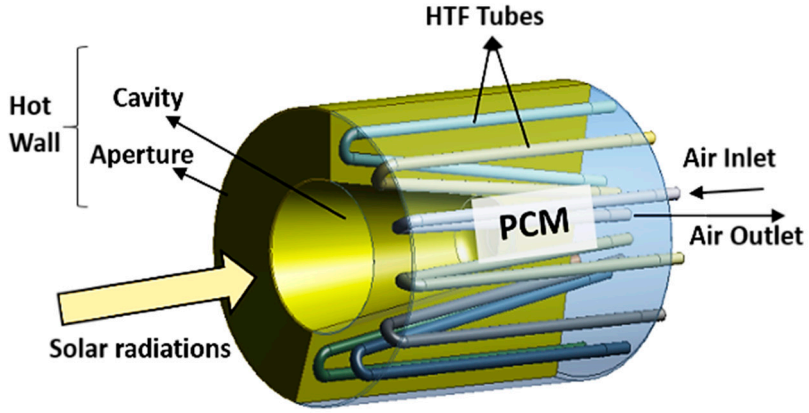

Figure 2. Scheme of the receiver geometry.

Table 2. Solar receiver main dimensions.

Receiver Dimensions	Value
Cylinder diameter (mm)	380
Cylinder length (mm)	440
Cavity maximum diameter (mm)	210
Cavity length (mm)	300
Tube length (mm)	826
Tube diameter (mm)	15
No. of tubes	12

Table 3. Selected Phase Change Material properties.

Mg56-Si44 wt %	Value
Density (kg/m^3)	1900
Heat of fusion (kJ/Kg)	757
Specific Heat (J/kg K)	632
Thermal Conductivity (W/m K)	70
Melting Temperature (K)	1219
PCM volume inside the receiver (L)	41

3. Model Setup

To simulate time-dependent charging and discharging process, 3D CFD simulations were carried out using the commercial CFD code ANSYS FLUENT 18.0. The receiver is supposed to be placed inside a sufficiently large enclosure. Complete receiver geometry and outer domain were considered. The computational domain consists of two solid domains, one for tubes material and another for the ceramic receiver container. Furthermore, three fluid domains were selected: one for the air flow inside tubes, one for the PCM into the receiver, and the last one for the outer domain. The external domain is four times longer and about three times larger than the receiver structure in order to take into consideration re-radiation and convection losses on the receiver front surface.

3.1. Selection of Suitable Models

Equations of continuity, momentum, and energy were applied. Adopting the simplified "solidification and melting" model to consider the phase transition, the conservation equations can be written for the PCM domain as follows:

$$\frac{\partial \rho}{\partial t} + \nabla \cdot (\rho \boldsymbol{u}) = 0 \quad (1)$$

$$\frac{\partial}{\partial t}(\rho \boldsymbol{u}) + \nabla \cdot (\rho \boldsymbol{u}\boldsymbol{u}) = -\nabla p + \nabla(\boldsymbol{\tau}) + \rho \boldsymbol{g} + \boldsymbol{F} \quad (2)$$

$$\frac{\partial(\rho H)}{\partial t} + \nabla \cdot (\rho \boldsymbol{u} H) = \nabla(k \nabla T) + \mathrm{S} \quad (3)$$

In the momentum Equation (2) $\boldsymbol{\tau}$, $\rho \boldsymbol{g}$, and $\boldsymbol{F}$ are the stress tensor, the gravitational body force, and the external body forces, respectively. In the energy Equation (3), k is the thermal conductivity, H the PCM enthalpy, and S the source term.

The "solidification and melting" model is based on the enthalpy-porosity technique. In such a technique, the coexistence of both liquid and solid phases in the PCM is considered as a porous region: a "mushy zone" [45]. The porosity of each element in the mushy zone is represented by the value of its liquid fraction β ranging from 0 to 1. The liquid fraction of element is defined as follows:

$$\beta = \begin{cases} 0 & if\ T < T_{solidus} \\ \frac{T - T_{solidus}}{T_{liquidus} - T_{solidus}} & if\ T_{liquidus} < T < T_{solidus} \\ 1 & if\ T > T_{liquidus} \end{cases} \quad (4)$$

The term $\boldsymbol{F}$ used in Equation (2) is the momentum sink, due to the reduced porosity in the mushy zone. It can be evaluated as:

$$\boldsymbol{F} = \frac{(1-\beta)^2}{\beta^3 + \varepsilon} A_{mush} \boldsymbol{u} \quad (5)$$

In Equation (5), ε is a small numerical constant used to prevent division by zero. Its value is generally 10^{-3}. A_{mush} is related to the mushy region and called the 'mushy region constant'. It represents the PCM motion resistance to the phase change. Higher value of this constant represents the faster velocity transition of liquid PCM to zero when it solidifies. In previous literature, a wide range of mushy region constants have been used, ranging from 10^3 to 10^{10}. In current simulations, the A_{mush} value was set to 10^5.

Concerning the enthalpy H, it is calculated as the sum of the sensible enthalpy h and the latent heat ΔH:

$$H = h + \Delta H \quad (6)$$

where ΔH can be written in terms of the latent heat of fusion:

$$\Delta H = \beta h_{sl} \quad (7)$$

Based on the phase of PCM, latent heat can vary from zero (solid PCM) to h_{sl} (liquid PCM).

Navier-Stokes equations were solved using the realizable k-ε turbulence model along with the solidification and melting model. The surface-to-surface radiation model was used along with the ray-tracing model to consider a uniform concentrated solar radiation impinging on the receiver hot wall and the loss effects connected with re-radiation, convection, and reflection. A second order upwind differencing scheme was employed for the discretization of convective terms in momentum and energy equations. Gravity effects were considered. The convergence criterion of the residuals was 10^{-4} (10^{-6} for energy).

3.2. Mesh and Boundary Conditions

In order to have an appropriate mesh size for an accurate solution, the grid was refined until heat transfer became mesh independent. For the grid independency, the symmetry of the receiver geometry was considered and only a section containing two tubes was taken into consideration. The domain is shown in Figure 3. The grid-independent solution was evaluated by gradually refining the mesh. Table 4 highlights average receiver hot wall temperature, WF outlet temperature, and PCM liquid fraction for four computational grids, respectively. Grid 3 was taken into consideration to create the

mesh for the complete receiver geometry. The overall final grid resolution had 1,367,211 nodes and 5,347,060 cells, as described in Table 5. Figures 4 and 5 show the receiver cross-section and a detail of the external domain mesh, coarser far from the receiver structure and refined near the device surface, respectively. In the case of the WF domain, hexahedral cells were assigned while tetrahedral cells were used for both the PCM domain inside the receiver tank and the outer domain. Relevant boundary conditions are:

- Lateral receiver surface: adiabatic wall;
- Receiver hot wall material: Silicon Carbide, 5 mm thickness;
- Tubes material: high-temperature super-alloy;
- WF and outside domain: air modeled as an ideal gas;
- WF mass flow rate: 0.1 kg/s;
- WF inlet temperature: 863 K;
- WF inlet pressure: 200 kPa;
- PCM: eutectic alloy.

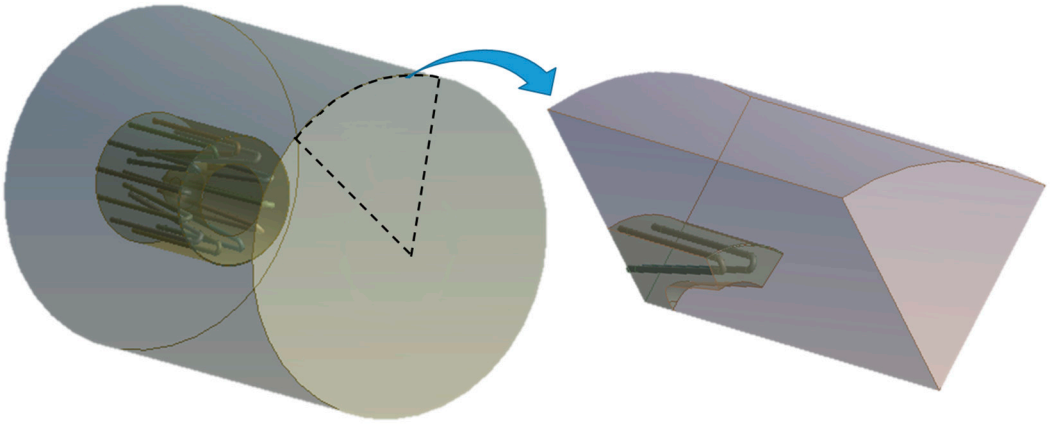

Figure 3. Scheme of the overall computational domain (**Left**) and details of the section used for the grid independency analysis (**Right**).

Table 4. Mesh independency analysis conducted on 1/6 of the overall domain.

Grid	No. of Cells	Average Hot Wall Temperature (K)	Outlet WF Temperature (K)	PCM Liquid Fraction (%)
1	445,065	1373	1093	83
2	687,087	1379	1099	88
3	1,852,346	1387	1106	93
4	4,037,561	1373	1099	92

Table 5. Final mesh of the overall geometry.

Domain	No. of Cells	Type of Cells
Tubes	159,994	Hexahedral
PCM	4,031,820	Tetrahedral
External domain	1,155,246	Tetrahedral

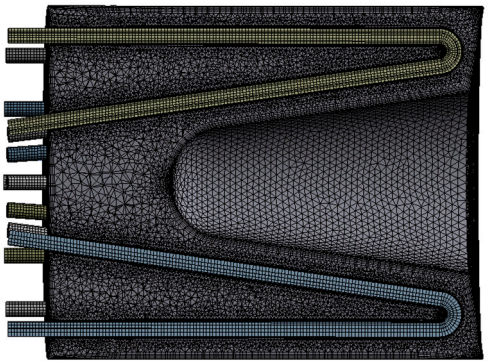

Figure 4. Mesh detail of the receiver cross-section.

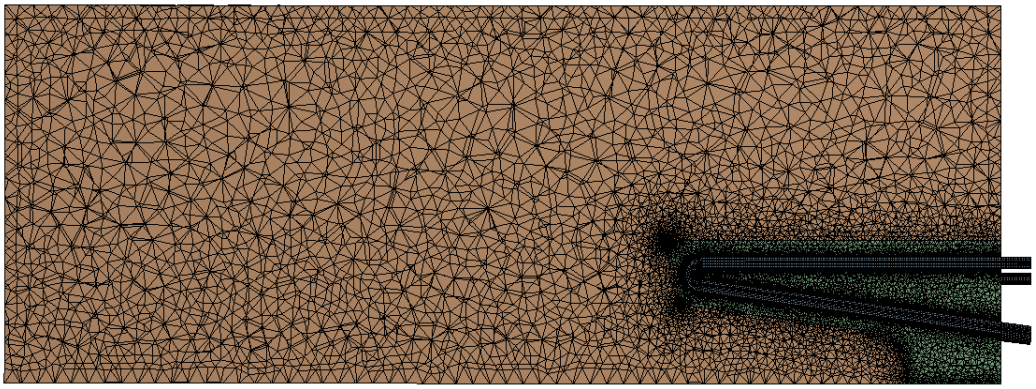

Figure 5. Mesh arrangement for the overall computational domain.

4. Storage Discharge and Charge Processes

Solidification and melting processes were simulated by means of CFD transient analyses to verify system short-term storage capabilities. Particularly, starting from the results achieved with a steady-state analysis of the device at nominal conditions and 500 kW/m^2 impinging concentrated solar radiation [38], a discharge process was simulated. The concentrated solar flux was set to zero for about 50 min to analyze the discharge behavior of the storage system at the worst boundary conditions (no concentrated solar radiation). The utilization of the heat stored in the PCM was observed at constant WF inlet conditions (0.1 kg/s, 863 K, and 200 kPa) since, currently, no assumptions for the off-design MGT behavior can be stated. Once the PCM solidification was completed, the storage charging process was simulated selecting a concentrated solar radiation of 500 kW/m^2. The charge phase was simulated for 130 min.

Figure 6 shows the variation of the average receiver hot wall temperature, the WF temperature at the outlet section, and the variation of the PCM liquid fraction during storage charging and discharging phases. During the discharge process, the hot wall temperature decreased gradually. The PCM was completely solidified after 48 min. The charging phase started after the complete solidification of the PCM. At the beginning of the charging process, a sharp increase in the hot wall temperature could be detected. Such an increase was due to the absorption of the concentrated solar radiation. Once the re-radiation effects started to balance the inlet solar power and the thermal power absorption in the receiver structure, the rate of increase of the hot wall temperature decreased rapidly. The PCM melting process increased gradually during the storage charge phase. After 130 min, a liquid fraction of 63% was detected.

Details related to the discharging process are reported in Figure 7. The process started with the PCM completely melted inside the receiver container. Temperature profiles and PCM liquid fraction

are shown for three time-steps: 400, 1700, and 2900 s from the process beginning. It is possible to see that the system grew cold starting from the front surface. In the meantime, the PCM started to solidify (400 s). The WF flowing inside the tubes continued to absorb heat from the PCM and a "mushy region" was generated near the tube walls. The solidification process continued from the aperture wall and the PCM solid portion grew, moving from the hot wall to the inner part or the receiver. After about 1000 s, a thick layer of solid PCM began to form around the WF tubes. The bottom wall of the cavity was at a slightly high temperature and the PCM near it remained in the liquid region. After about 2100 s, most of the PCM was solid. The solidification process was completed after 2900 s.

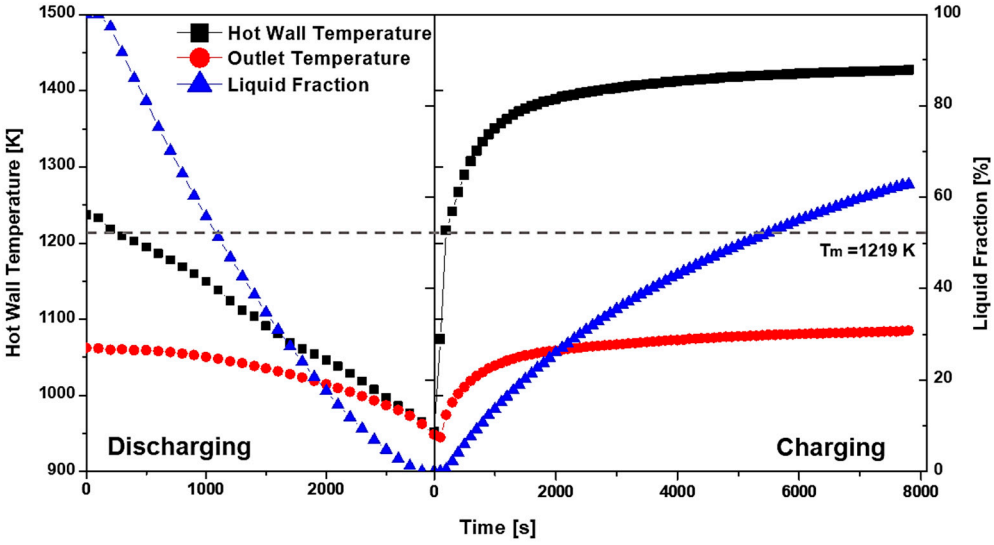

Figure 6. Average receiver hot wall temperature, working fluidoutlet temperature, and PCM liquid fraction during charging and discharging processes.

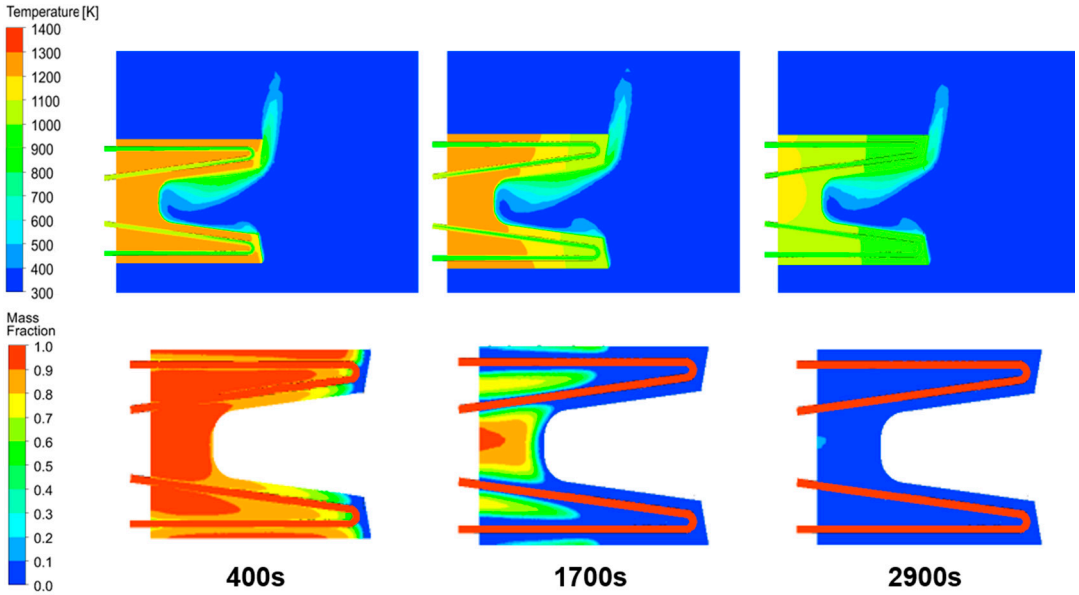

Figure 7. Contours of temperature and PCM liquid fraction during the discharge process.

The small difference in the heat exchange process detected between the bottom and the upper part of the receiver container could be connected with the effect of external convection on the receiver front surface. The external air into the cavity became hotter and lighter by absorbing heat from the

cavity walls and then flowing upward to the upper wall of the cavity. A relative stagnation region was observed at the upper middle section of the cavity. The hot air then flowed out of the cavity through the upper half of the aperture. The relatively lowest temperature was detected near the bottom of the cavity.

After 2900 s, the charging process took place. A constant concentrated solar radiation of 500 kW/m^2 was applied for the entire charge phase. The PCM inside the cylinder absorbed heat from the receiver hot wall surface. Initially, a rapid temperature increase could be detected. Such an increase was due to the relevant imbalance between impinging solar power and power lost at the receiver front surface. In Figure 8, details related to the charging phase are reported. The process started when the PCM was completely solid inside the receiver container.

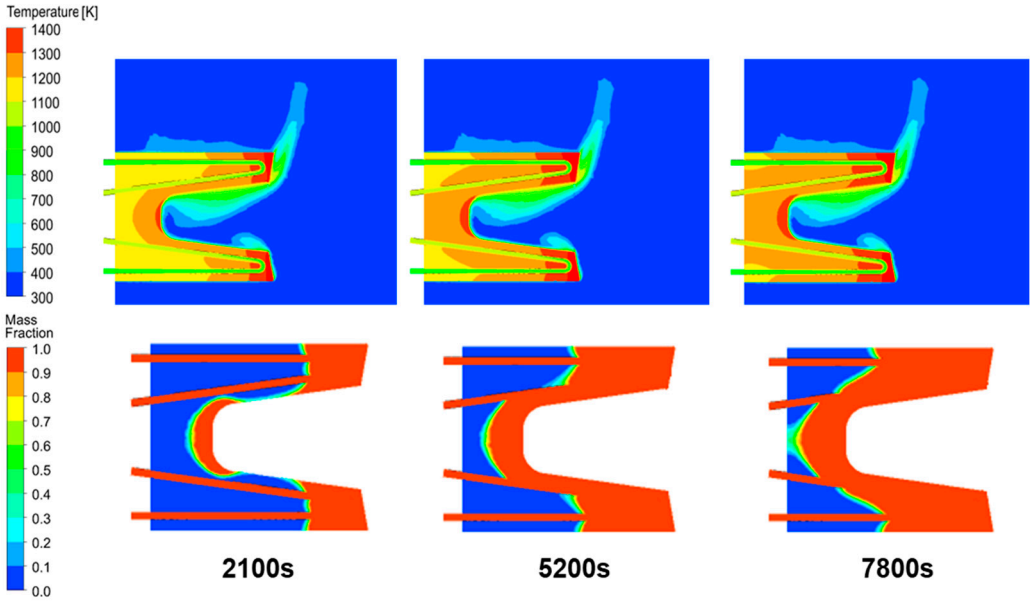

Figure 8. Contours of temperatures and PCM liquid fraction during the charge process.

Temperature profiles and PCM liquid fractions are shown for three time-steps: 2100, 5200, and 7800 s, respectively, after the charge process begins. It can be noticed that high temperature regions were close to the front hot wall and in the cavity bottom part. Thermal gradients became gradually more evident and the heating process continued toward the back surface of the receiver. The PCM started to melt from the aperture wall and cavity bottom surface and about half of the PCM was melted after 2000 s. A liquid fraction of 64% was detected after 7800 s. The melting on the upper half of the receiver was slightly more evident and this pattern agrees with what is intuitively expected.

During the simulations, the temperature and liquid fraction of the entire PCM volume were monitored in six different sections along the receiver container axis. The distances were taken from the cavity opening on the front surface of the solar receiver. Figure 9 illustrates temperature profiles of the system for these six sections during discharge and charge processes. Since the lateral surface of the container is considered perfectly insulated, the heat transfer takes place between the hot wall and the PCM inside the container and between the PCM and the WF that flows inside tubes.

As expected, during the storage discharge, more heat was released from the section near the front receiver wall and the PCM solidified quickly. Cross-sections far from the front wall were at higher temperatures. Particularly, the section at 410 mm from the front surface remained at liquid state for about 2600 s. During the charging phase, the temperature of the receiver front wall became higher, therefore sections near the front surface showed a higher temperature than sections selected in the back part of the container. Temperature contours at several receiver cross-sections are reported in Figure 10. Natural convection of air was evident inside the cavity.

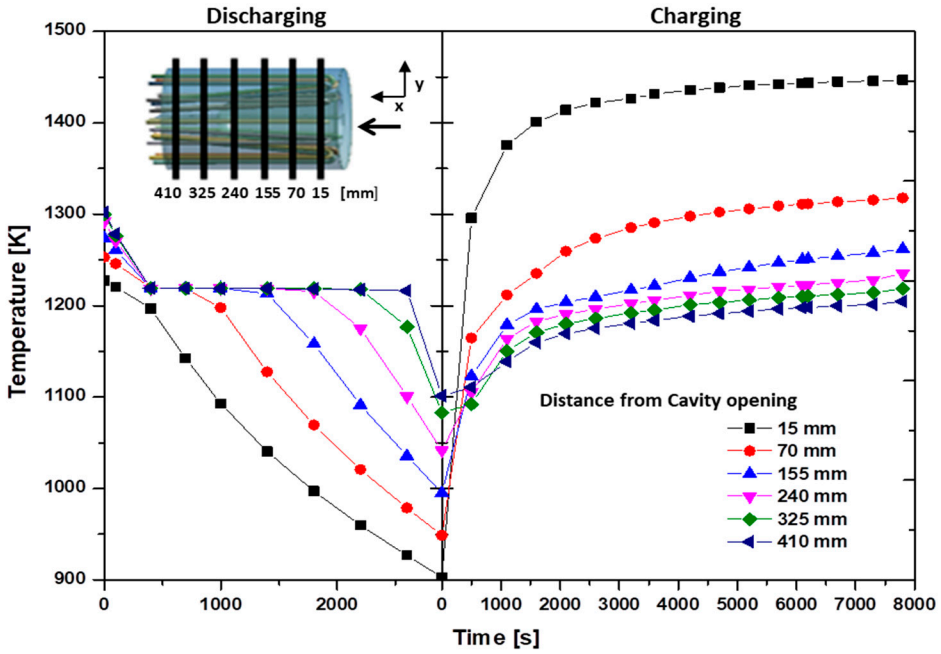

Figure 9. Average temperatures at several sections along the x-axis.

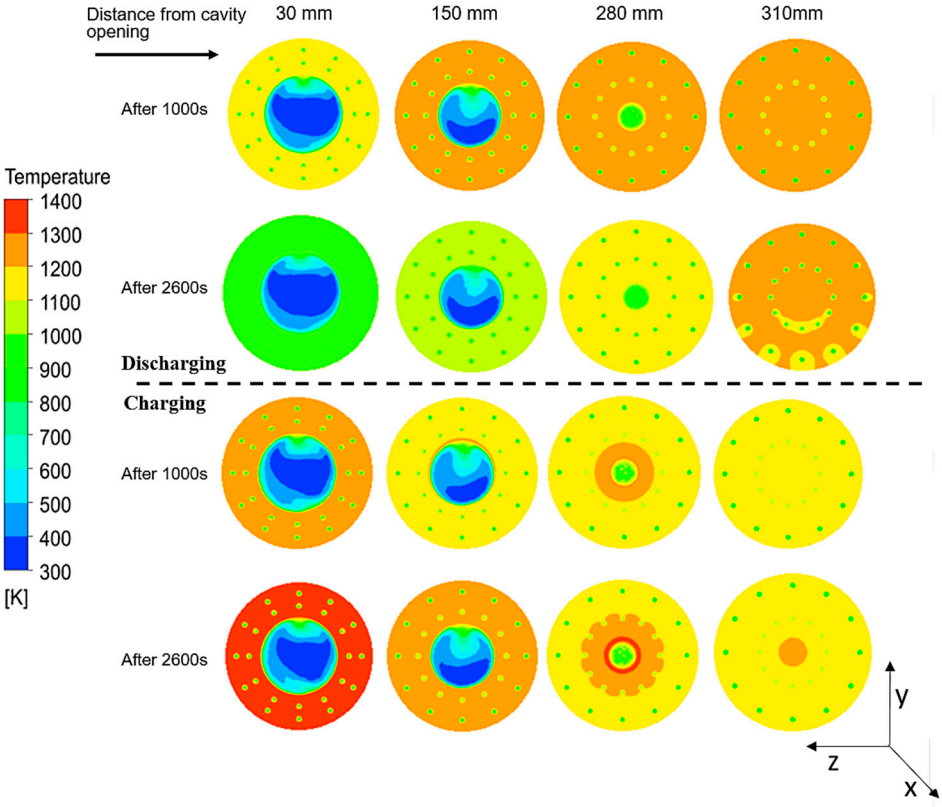

Figure 10. Temperature contours of several sections taken along the solar receiver axis during charging and discharging phases. Distance are taken from the cavity opening.

5. Conclusions

A novel solar receiver integrated with a short-term storage system based on PCMs was analyzed by means of CFD methods. Particularly, the device storage capabilities were detected to check the component potential applications at high temperatures in small-scale Dish-MGT plants.

A severe discharge process was simulated starting from the nominal operating conditions. Transient simulations were performed, setting the impinging concentrated solar radiation to zero. The discharge process was analyzed for about 50 min. Once the PCM solidification was completed, the storage charging process was simulated, selecting an impinging concentrated solar radiation of 500 kW/m^2. The charge phase was simulated for 130 min.

The results show a good behavior of the component which could stabilize the WF outlet temperature for about 30 min, preventing MGT performance drops and reducing the possibility of engine damages. Such numerical results open the way to medium- and high-temperature experimental tests on a lab-scale prototype to verify the real component capabilities.

Acknowledgments: The work is an extended version of the paper presented at the 4th International Conference on Energy and Environment Research (ICEER 2017) held in Porto, Portugal and published in Energy Procedia [36]. Authors gratefully acknowledge University of "ROMA TRE" for the support.

Author Contributions: Ambra Giovannelli conceived the paper; Ambra Giovannelli and Muhammad Anser Bashir designed simulation studies; Muhammad Anser Bashir performed simulation campaigns; Ambra Giovannelli and Muhammad Anser Bashir analyzed simulation results and wrote the paper.

Conflicts of Interest: The authors declare no conflicts of interest.

References

1. Sylvain, Q.; Matthew, O. Rural electrification through decentralized concentrating solar power: Technological and socio-economic aspects. *J. Sustain. Dev. Energy Water Environ. Syst.* **2013**, *1*, 199–212.
2. International Renewable Energy Agency (IRENA). *Accelerating Renewable Mini-Grid Deployment: A Study on the Philippines*; International Renewable Energy Agency (IRENA): Abu Dhabi, UAE, 2017.
3. Chung, D.; Davidson, C.; Fu, R.; Ardani, K.; Margolis, R. *US Photovoltaic Prices and Cost Breakdowns. Q1 2015 Benchmarks for Residential, Commercial, and Utility-Scale Systems*; National Renewable Energy Lab. (NREL): Golden, CO, USA, 2015.
4. Gaglia, A.G.; Lykoudis, S.; Argiriou, A.A.; Balaras, C.A.; Dialynas, E. Energy efficiency of PV panels under real outdoor conditions—An experimental assessment in Athens, Greece. *Renew. Energy* **2017**, *101* (Suppl. C), 236–243. [CrossRef]
5. Bashir, M.A.; Ali, H.M.; Ali, M.; Siddiqui, A.M. An Experimental Investigation of Performance of Photovoltaic Modules in Pakistan. *J. Therm. Sci.* **2015**, *19* (Suppl. 2), S525–S534. [CrossRef]
6. Bashir, M.A.; Ali, H.M.; Ali, M.; Khalil, S.; Siddiqui, A.M. Comparison of Performance Measurements of Photovoltaic Modules during Winter Months in Taxila, Pakistan. *Int. J. Photoenergy* **2014**, *2014*, 898414. [CrossRef]
7. Giovannelli, A. State of the art on small-scale concentrated solar power plants. *Energy Procedia* **2015**, *82*, 607–614. [CrossRef]
8. Blanco, M.; Santigosa, L.R. *Advances in Concentrating Solar Thermal Research and Technology*; Woodhead Publishing: Duxford, UK, 2017; ISBN 978-0-08-100516-3.
9. Sugarmen, C.; Ring, A.; Buck, R.; Heller, P.; Schwarzbözl, P.; Téllez, F.; Marcos, M.J.; Enrile, J. Solar-hybrid gas turbine power plants—Test results and market perspective. In Proceedings of the ISES Solar World Congress, Gothenburg, Sweden, 14–19 June 2003; pp. 14–19.
10. OMSOP EU Project. Available online: https://omsop.serverdata.net/Pages/Home.aspx (accessed on 11 April 2017).
11. Dickey, B. Test results from a concentrated solar microturbine Brayton Cycle integration. In Proceedings of the ASME 2011 Turbo Expo: Turbine Technical Conference and Exposition Vancouver, BC, Canada, 6–10 June 2011.
12. Winter, C.J.; Sizmann, R.L.; Vaunt-Hull, L.L. *Solar Power Plants: Fundamentals, Technology, Systems, Economics*; Springer: Berlin/Heidelberg, Germany, 1991; ISBN 3-540-18897-5.

13. Lanchi, M.; Montecchi, M.; Crescenzi, T.; Mele, D.; Miliozzi, A.; Russo, V.; Mancini, R. Investigation into the coupling of micro gas turbines with CSP technology: OMSoP project. *Energy Procedia* **2015**, *69*, 1317–1326. [CrossRef]
14. Harris, J.A.; Lenz, T.G. Thermal performance of solar concentrator/cavity receiver systems. *Sol. Energy* **1985**, *34*, 135–142. [CrossRef]
15. Prakash, M.; Kedare, S.B.; Nayak, J.K. Investigations on heat losses from a solar cavity receiver. *Sol. Energy* **2009**, *83*, 157–170. [CrossRef]
16. Paitoonsurikarn, S.; Lovegrove, K.; Hughes, G.; Pye, J. Numerical investigation of natural convection loss from cavity recievers in solar dish applications. *J. Sol. Energy Eng.* **2011**, *133*, 021004. [CrossRef]
17. Ho, C.K.; Iverson, B.D. Review of high-temperature central receiver designs for concentrating solar power. *Renew. Sustain. Energy Rev.* **2014**, *29*, 835–846. [CrossRef]
18. Kribus, A.; Doron, P.; Rubin, R.; Reuven, R.; Taragan, E.; Duchan, S.; Karni, J. Performance of the directly-irradiated annular pressurized receiver (DIAPR) operating at 20 bar and 1200 °C. *J. Sol. Energy Eng.* **2001**, *123*, 10–17. [CrossRef]
19. Xu, G.; Wang, Y.; Quan, Y.; Li, H.; Li, S.; Song, G.; Gao, W. Design and characteristics of a novel tapered tube bundle receiver for high-temperature solar dish system. *Appl. Therm. Eng.* **2015**, *91*, 791–799. [CrossRef]
20. Aichmayer, L.; Spelling, J.; Laumert, B. Preliminary design and analysis of a novel solar receiver for a micro gas-turbine based solar dish system. *Sol. Energy* **2015**, *114*, 378–396. [CrossRef]
21. Del Río, A.; Korzynietz, R.; Brioso, J.; Gallas, M.; Ordóñez, I.; Quero, M.; Díaz, C. Soltrec–pressurized volumetric solar air receiver technology. *Energy Procedia* **2015**, *69*, 360–368. [CrossRef]
22. Wu, W.; Trebing, D.; Amsbeck, L.; Buck, R.; Pitz-Paal, R. Prototype testing of a centrifugal particle receiver for high-temperature concentrating solar applications. *J. Sol. Energy Eng.* **2015**, *137*, 041011. [CrossRef]
23. Mande, O.; Miller, F. Window Design for a Small Particle Solar Receiver. In Proceedings of the 9th Annual International Energy Conversion Engineering Conference, San Diego, CA, USA, 31 July–3 August 2011.
24. Röger, M.; Pfänder, M.; Buck, R. Multiple air-jet window cooling for high-temperature pressurized volumetric receivers: Testing, evaluation, and modeling. *J. Sol. Energy Eng.* **2006**, *128*, 265–274. [CrossRef]
25. Wang, W.; Laumert, B.; Xu, H.; Strand, T. Conjugate heat transfer analysis of an impinging receiver design for a dish-Brayton system. *Sol. Energy* **2015**, *119*, 298–309. [CrossRef]
26. Poživil, P.; Steinfeld, A. Integration of a pressurized-air solar receiver array to a gas turbine power cycle for solar power applications. *J. Sol. Energy Eng.* **2017**, *139*, 041007. [CrossRef]
27. Neber, M.; Lee, H. Design of a high temperature cavity receiver for residential scale concentrated solar power. *Energy* **2012**, *47*, 481–487. [CrossRef]
28. Lim, S.; Kang, Y.; Lee, H.; Shin, S. Design optimization of a tubular solar receiver with a porous medium. *Appl. Therm. Eng.* **2014**, *62*, 566–572. [CrossRef]
29. Lukin, E.S.; Sysoev, É.P.; Poluboyarinov, D.N. The creep and long-term strength of alumina ceramics. *Refractories* **1976**, *17*, 757–760. [CrossRef]
30. Dreshfield, R.L. *Long Time Creep Rupture of Haynes Alloy 188*; Minerals, Metals and Materials Society, Ed.; National Aeronautics and Space Administration, Lewis Research Center: Cleveland, OH, USA, 1996.
31. Bradshow, R.W.; Goods, S.H. *Corrosion Resistance of Stainless Steels During Thermal Cycling in Alkali Nitrate Molten Salts*; Sandia Report, Sand 2001-8518; Sandia National Laboratories: Albuquerque, NM, USA, 2001.
32. Meetam, G.W.; Van de Voorde, M.H. *Materials for High Temperature Engineering Applications*; Springer: Berlin/Heidelberg, Germany, 2000; ISBN 978-3540668619.
33. American Iron and Steel Institute. *High-Temperature Characteristics of Stainless Steels, A Designers' Handbook Series N. 9004*; Nickel Development Institute: Toronto, ON, Canada, 1972.
34. Basuki, E.A.; Prajitno, D.H.; Muhammad, F. Alloys developed for high temperature applications. *AIP Conf. Proc.* **2017**, *1805*, 020003. [CrossRef]
35. Boch, P.; Niepce, J.C. *Ceramic Materials: Processes, Properties and Applications*; Wiley: London, UK, 2010; ISBN 9781905209231.
36. Giovannelli, A.; Bashir, M.A. Development of a solar cavity receiver with a short-term storage system. *Energy Procedia* **2017**, *136*, 258–263. [CrossRef]
37. Giovannelli, A.; Bashir, M.A.; Archilei, E.M. High Temperature Solar Receiver Integrated with a Short-Term Storage System. *AIP Conf. Proc.* **2017**, *1850*, 050001. [CrossRef]

38. Giovannelli, A.; Bashir, M.A. High-Temperature Cavity Receiver Integrated with a Short-Term Storage System for Solar MGT's: Heat Transfer Enhancement. *Energy Procedia* **2017**, *126*, 557–564. [CrossRef]
39. Cárdenas, B.; León, N. High temperature latent heat thermal energy storage: Phase change materials, design considerations and performance enhancement techniques. *Renew. Sustain. Energy Rev.* **2013**, *27*, 724–737. [CrossRef]
40. Sharma, A.; Tyagi, V.V.; Chen, C.R.; Buddhi, D. Review on thermal energy storage with phase change materials and applications. *Renew. Sustain. Energy Rev.* **2009**, *13*, 318–345. [CrossRef]
41. Murat, M.K. High-temperature phase change materials for thermal energy storage. *Renew. Sustain. Energy Rev.* **2010**, *14*, 955–970.
42. Liu, M.; Saman, W.; Bruno, F. Review on storage materials and thermal performance enhancement techniques for high temperature phase change thermal storage systems. *Renew. Sustain. Energy Rev.* **2012**, *16*, 2118–2132. [CrossRef]
43. Kotzé, J.P.; von BackstrÃḷm, T.W.; Erens, P.J. High temperature thermal energy storage utilizing metallic phase change materials and metallic heat transfer fluids. *J. Sol. Energy Eng.* **2013**, *135*, 035001. [CrossRef]
44. Wang, Z.; Wang, H.; Li, X.; Wang, D.; Zhang, Q.; Chen, G.; Ren, Z. Aluminum and silicon based phase change materials for high capacity thermal energy storage. *Appl. Therm. Eng.* **2015**, *89*, 204–208. [CrossRef]
45. Voller, V.R.; Prakash, C. A fixed grid numerical modelling methodology for convection diffusion mushy region phase-change problems. *Int. J. Heat Mass Transf.* **1987**, *30*, 1709–1719. [CrossRef]